Iris Biometrics: Synthesis of Degraded Ocular Images

Luís Cardoso, André Barbosa, Frutuoso Silva, António M. G. Pinheiro, *Member, IEEE*, and Hugo Proença

Abstract—Iris recognition is a popular technique for recognizing humans. However, as is the case with most biometric traits, it is difficult to collect data that are suitable for use in experiments due to three factors: 1) the substantial amount of data that is required; 2) the time that is spent in the acquisition process; and 3) the security and privacy concerns of potential volunteers. This paper describes a stochastic method for synthesizing ocular data to support experiments on iris recognition. Specifically, synthetic data are intended for use in the most important phases of those experiments: segmentation and signature encoding/matching. The resulting data have an important characteristic: they simulate image acquisition under uncontrolled conditions. We have experimentally confirmed that the proposed strategy can mimic the data degradation factors that usually result from such conditions. Finally, we announce the availability of an online platform for generating degraded synthetic ocular data. This platform is freely accessible worldwide.

Index Terms—Data sets, data synthesis, iris biometrics.

I. INTRODUCTION

FOR YEARS, bodily features such as the face, fingerprint, and iris have been used for the purpose of recognition. Since the mid-nineteenth century, when Alphonse Bertillon proposed using body measurements to identify criminals [9], *biometrics* has been extensively used in law enforcement to identify criminals and to establish identity in a broad range of applications (e.g., refugee control and computer logins). Various traits have been considered to have potential for biometric recognition because they satisfy four requirements: 1) universality, meaning that each person should possess the characteristic; 2) distinctiveness, meaning that any two persons should be sufficiently differentiable by the selected characteristic; 3) permanence, meaning that the characteristic should be invariant over a period of time; and 4) collectability, meaning that the characteristic can be measured quantitatively.

Among the various traits used for identification, ocular biometrics has advanced rapidly as a result of progress in the field of iris recognition [14]. The iris is the annular structure in the eye surrounding the pupil. It regulates the size of the pupil, con-

trolling the amount of incident light on the retina. The surface of the iris exhibits a rich texture because of the numerous structures on its anterior layers. The randotypic morphogenesis of its textural relief and its stability over one's lifetime have led to the popularity of the iris as a biometric, which has been the focus of a large number of research studies (Bowyer *et al.* [1]). To support such research efforts, various data sets of iris images were used in the development of recognition strategies, including the CASIA [8], ICE [13], WVU [19], BATH [25], MMU [12], UPOL [5], and UBIRIS [18] data sets. Aside from the iris, other ocular traits such as the retina [27], sclera [29], and periocular region [14], have been investigated for human recognition. Recently, several studies have proposed the use of artificial iris models to support biometric experiments (e.g., [30] and [2]), simulating iris data that resemble real data that are acquired under typical acquisition setups (i.e., under heavily controlled conditions).

Most of the above mentioned studies aim to create data that resemble iris data that are acquired with near infrared light. However, even though iris recognition at visible wavelengths has been the scope of several studies [17], no previous efforts were concentrated on synthesizing visible wavelength (VW) iris data. When compared to iris data that were acquired using NIR light, two major discriminating features should be emphasized: 1) The main pigment in the human iris (brown-black melanin) retains most of its radiative fluorescence under visible wavelengths, enabling the capture of more detail but also noisy artifacts (specular and diffuse reflections) in VW; and 2) Significantly greater amounts of light are demanded for the proper acquisition of heavily pigmented irises, making their textures difficult to acquire.

In this paper, we propose an automated strategy for synthesizing ocular data (henceforth designated as NOISYRIS) by simulating its acquisition under visible wavelengths and uncontrolled protocols. Hence, when compared to previously published methods, NOISYRIS images possess certain differences: 1) They simulate acquisition under different types and numbers of light sources, including nonhomogenous differences in lighting, reflections and shadows; 2) They simulate acquisition from off-angle cameras and at different gaze angles; 3) They simulate acquisition from varying distances; 4) They simulate various types of iris occlusions that result from eyelids, eyelashes and glasses; 5) They simulate acquisition from moving subjects, leading to optically defocused and motion-blurred images; and 6) They enable the conduction of unbiased experiments, because each image has a corresponding grayscale mask in which each component appears at a different intensity (iris, pupil, eyelids, eyelashes, sclera, and glasses). This type of mask is extremely useful for encoding/matching strategy evaluations, which can guarantee that segmentation is correctly performed.

L. Cardoso, A. Barbosa, F. Silva, and H. Proença are with the Department of Computer Science, IT-Instituto de Telecomunicações, University of Beira Interior, 6200-Covilhã, Portugal (e-mail: lcardoso@di.ubi.pt; abarbosa@di.ubi.pt; fsilva@di.ubi.pt; hugomcp@di.ubi.pt).

A. M. G. Pinheiro is with the Remote Sensing Unit, University of Beira Interior, 6200-Covilhã, Portugal (e-mail: pinheiro@ubi.pt).
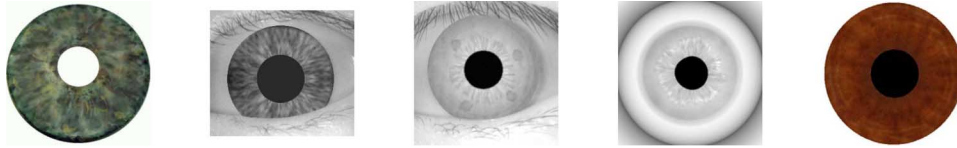
Fig. 1.   Examples of synthetic iris images attained by the methods summarized in this section. The far left image regards the technique proposed by Lefohn [10]. Next, from left to right, images regard the methods of Cui [2], Shah [21], Zuo [30], and Wei [28].

The remainder of this paper is organized as follows: Section II summarizes the most relevant strategies for the synthesis of iris data. Section III provides a description of the proposed method and formalizes the synthesis and rendering strategies used along with the data variability factors observed. Section V presents an empirical validation procedure for the NOISYRIS data. Finally, conclusions are given in Section VI.

II. RELATED WORK

Various studies have been published on the topic of iris synthesis. In this section, we summarize the most important studies and give examples of the appearance of the data that were generated in Fig. 1.

Lefohn *et al.* [10] proposed a method for creating and rendering realistic-looking irises by adding layers iteratively to the model and rendering the intermediate results. This approach allows incremental definition of the iris texture to be developed, using single layers that are taken from a library of standard textures. This method is useful in applications ranging from entertainment to ocular prosthetics. Cui *et al.* [2] proposed an iris synthesis method that is based on the analysis of principal components (PCA). Cui *et al.* used an iris recognition algorithm based on PCA that operates on real images and extracts a set of global feature vectors. These vectors are then used in the image reconstruction process. Iris samples that belong to the same class are constructed by allowing their coefficients to lie in the same sphere, centered at a sample iris image in a high-dimensional space. To simulate different classes, the authors searched in a limited high-dimensional space. The authors concluded that super-resolution methods enhance the quality of the resulting images. Theoretical analysis and experimental results revealed that the synthetic data produced mimic the traditional within-class and interclass distances found in real iris data. Shah *et al.* [21] proposed a technique for creating digital versions of iris images, which was used to evaluate the performance of iris recognition algorithms. The scheme used by Shah *et al.* was divided into two phases: 1) Initially, a Markov Random Field model generated a background texture that represented the global iris appearance; 2) Next, several iris features such as radial and concentric furrows, collarettes and crypts, were embedded in the texture field. Experiments with iris recognition algorithms validated the potential of this scheme. Zuo *et al.* [30] proposed an anatomy-based method for synthesizing iris images. The purpose of this method was to provide academia and industry with a large data set for iris recognition algorithm testing. After performing a comparison between the results that were observed for real and synthetic iris images, a concern about the bias that might be introduced using synthetic data was also revealed. The

comparison was quantified at three different levels: 1) global layout, 2) features of fine iris textures, and 3) recognition performance, including performance extrapolation capabilities. In most of the cases studied, the results confirmed the authors' expectations of finding a strong similarity between real data and the synthetic iris data that were generated through the use of their model-based approach. Wei *et al.* [28] proposed an iris synthesis method and claimed to possess an effective paradigm for synthesizing large iris databases with the purpose of overcoming the problems of data collection. Patch-based sampling was initially employed to create prototypes. From each prototype, a number of intraclass samples were derived. Experiments showed that the synthetic irises preserved the major properties of real irises and retained controllable statistics, meaning that they were suitable for algorithm evaluation. For comprehensibility, Table I, summarizes the above-mentioned methods, the major techniques of which they are composed, and the types of data that they aim to simulate.

III. PROPOSED METHOD

A. Iris Synthesis

The iris texture has a chaotic appearance and predominantly randotypic morphogenesis. Accordingly, a stochastic method is proposed, which generates each fiber of the iris in an isolated manner and groups them into *layers*, that are further superimposed. The process is divided into two major phases: 1) a set of layers is synthesized; and 2) the collarette is created, using an irregular polygon shape. Layers are merged using the Lefohn *et al.* [10] method, which was attained the best results, both by visual inspection and according to the results of iris recognition algorithms. A color c at each point of the surface is obtained by:

$$c = (1 - \alpha) \cdot r_d + \alpha \cdot c_p \cdot r_l, \tag{1}$$

where r_d is the result of shooting a ray in the transmitted direction (using refraction index of 1.0 for all layers), c_p is the paint color, r_l is the result of shooting a ray from a light source and α is an opacity value.

1) Fibers: Each fiber of the iris has a singular color distribution, depending on its composition in terms of minerals and of muscle contractions. Here, the shape of the fiber is firstly defined and each of its segment associated to a color. Let U be a random variable that follows an uniform distribution, i.e., $U \sim \mathbb{U}(0, 1)$. θ_i denote a set of angles in k regular intervals, i.e., $\theta_i = i \cdot (2\pi/k), i \in \{0, \dots k\}$. Let $\rho_i = \kappa \cdot (u_i - \delta)$, where u_i are realizations of U. Hence, ρ_i is a function of u_i, scaled by κ and translated by δ. To assure a closed contour, the constraint

TABLE I
SUMMARY OF THE PREVIOUSLY PUBLISHED IRIS SYNTHESIS METHODS

Method	Type Data	Summary
Lefohn *et al.* [10]	Color	Superimposition of several layers (12 to 50); All layers were taken from ocularists standard library of textures; Requires human intervention.
Cui *et al.* [2]	Grayscale	Based on Principal Component Analysis (PCA) method; Uses an iris recognition algorithm based on PCA to extract global features from a real iris data; Linear combination of the extracted features to synthesizes iris data; Super-resolution techniques for enhancement.
Shah *et al.* [21]	Grayscale	Markov Random Field model used as background; Creates a variety of iris features such as radial and concentric furrows, collarette and crypts.
Zuo *et al.* [30]	Grayscale	Anatomy-based method; Uses 40 parameters to control the number of fibers and all the shapes needed; The fibers are produced in 3D.
Wei *et al.* [28]	Grayscale / Color	Applies patch-based sampling to create prototypes based on real iris; Creates a number of intra-class images derived from each prototype.

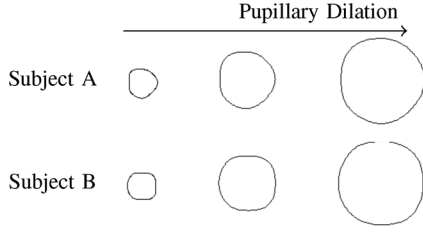Pupillary Dilation →

Subject A

Subject B

Fig. 2. Examples of two pupillary boundaries at different levels of dilation. The shape of the pupil is an intrinsic feature of each individual and previous studies pointed that it might be used as soft biometric trait.

$\rho_k = \rho_0$ is defined. The coordinates of the pupillary boundary $\{(x_i^{(p)}, y_i^{(p)})\}$ are given by:

$$x_i^{(p)} = \frac{s_h}{2} + o_h + (\rho_i + q) \cdot \cos(\theta_i) \qquad (2)$$

$$y_i^{(p)} = \frac{s_v}{2} + o_v + (\rho_i + q) \cdot \sin(\theta_i), \qquad (3)$$

where $q = r_m^{(p)} + (r_M^{(p)} - r_m^{(p)}) \cdot \nu$, $r_m^{(p)}$ and $r_M^{(p)}$ are the minimum and maximum allowed distances from the pupillary center of mass to points at the boundary, for a pupil aperture ν (diameter, in pixels). o_h and o_v are offsets that control the position of the pupillary boundary in the image (of dimension $s_h \times s_v$). Next, $\{(x_i^{(p)}, y_i^{(p)})\}$ are interpolated by cosine approximation to smooth the boundary and attain a more a realistic result. Fig. 2 illustrates two different shapes of pupils that resemble the shapes of biological pupils. It should be noted that the shape of the pupil tends to be invariant with respect to pupil aperture, constituting a feature intrinsic to each individual.

According to evidence from the literature, the scleric boundary can be faithfully approximated by ellipses:

$$x_i^{(s)} = \frac{s_h}{2} + r_M^{(i)} \cdot \cos(\theta_i) \qquad (4)$$

$$y_i^{(s)} = \frac{s_v}{2} + r_m^{(i)} \cdot \sin(\theta_i), \qquad (5)$$

where $r_m^{(i)}$ and $r_M^{(i)}$ denote the minimum and maximum lengths of radial line segments in the iris.

Next, fibers are synthesized and placed between the pupillary and scleric boundaries. As previously, the stochastic process is based in the uniform distribution $U \sim \mathbb{U}(0,1)$ and starts by defining the colors of each segment of the fibers:

$$c_{ij} = \frac{(n \cdot (0.55 + 0.4 \cdot u_{ij}) - 1) \cdot C_{v_{ij}}}{n - 1}, \qquad (6)$$

where c_{ij} is the color of the jth segment of the ith fiber, n is the number of intensities per channel (256 in our experiments), u_{ij} and v_{ij} are realizations of U, and $C_{v_{ij}}$ is a color value, drew from a set of predefined colors (Appendix A). The insight is similar to the used in the pupillary boundary: r defines the length sampling step ($r = 1/4$ in our experiments), $x_j^{(i)} = j \cdot r$ and $y_0^{(i)} = 0$, $y_j^{(i)} = r_m^{(p)} \cdot u_j$ (u_j a realization of U). The coordinates of the ith iris fiber are given by:

$$x_{ij}^{(f)} = \sqrt{\left(x_i^{(s)} - \frac{s_h}{2}\right)^2 + \left(y_i^{(s)} - \frac{s_v}{2}\right)^2} + \sqrt{\left(x_i^{(p)} - \frac{s_h}{2}\right)^2 + \left(y_i^{(p)} - \frac{s_v}{2}\right)^2} \cdot \left(1 - x_j^{(i)}\right) \quad (7)$$

$$y_{ij}^{(f)} = y_j^{(i)}. \qquad (8)$$

$\{(x_{ij}^{(f)}, y_{ij}^{(f)})\}$ are interpolated by cosine approximation to smooth the shape and then rotated:

$$x_{ij}'^{(f)} = \frac{s_h}{2} + x_{ij}^{(f)} \cdot \cos(\theta_i) - y_{ij}^{(f)} \cdot \sin(\theta_i) \qquad (9)$$

$$y_{ij}'^{(f)} = \frac{s_v}{2} + x_{ij}^{(f)} \cdot \sin(\theta_i) + y_{ij}^{(f)} \cdot \cos(\theta_i). \qquad (10)$$

Finally, the set of coordinates $\{(x_{ij}'^{(f)}, y_{ij}'^{(f)})\}$ is associated to a color c_{ij} (6). Fig. 3 illustrates an example of the fibers in a single layer of the iris, showing evidence of highly varying shapes between fibers. At the end, five layers (blurred by a 5 × 5 Gaussian kernel) are superimposed to obtain the final appearance of the iris texture.

Deformations in the iris texture due to the pupillary dilation are nonlinear and have different magnitudes and directions, according to muscular movements. Such nonlinear changes were modeled by random Euclidean warping processes. Let I_p be a
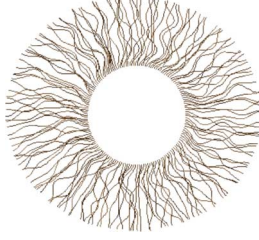
Fig. 3. Example of the fibers generated for a single layer of the iris. Each fiber is created isolatedly, rotated, and translated into a position delimited by the pupillary and scleric boundaries.

2-D patch of the iris texture with n pixels. Four parameters were used to transform I_p into its warped version I_p', with homogenous coordinates given by:

$$(x_i', y_i') = \begin{bmatrix} \rho cos(\theta) & \rho sin(\alpha) & t_x \\ -\rho sin(\theta) & \rho cos(\alpha) & t_y \\ 0 & 0 & 1 \end{bmatrix} \cdot \begin{bmatrix} x_i \\ y_i \\ 1 \end{bmatrix}, \qquad (11)$$

where (x_i, y_i) are the pixel positions in I_p and ρ, α, t_x and t_y denote the scale, rotation and translation parameters, drew from Gaussian distributions.

2) Collarette: Considering its highly irregular shape, the method that defines the collarette boundary has a singularity: instead of defining a 2-D region with a single shape, several shapes of different sizes were used to define a surface that simulates the flaws (crypts) behind the tissue. Let $\theta_i = i \cdot (2\pi/k)$, $i \in \{0, \ldots, k\}$ be the angle values regularly spaced ($k = 64$ in our experiments). ρ_i represent the magnitude values, i.e., $\rho_i = (u_i - 0.5) \cdot ((r_m^{(i)} - r_M^{(p)})/2)$, keeping the notation similar to the previously used. A set of 3-D coordinates of the collarette boundary is obtained:

$$x_{ij}^{(c)} = \frac{s_h}{2} + o_h + a_h \cdot \cos(\theta_i) \qquad (12)$$

$$y_{ij}^{(c)} = \frac{s_v}{2} + o_v + a_v \cdot \sin(\theta_i) \qquad (13)$$

$$z_{ij}^{(c)} = (j\%2) \cdot c_M - c_i^{(c)}, \qquad (14)$$

where $j \in \{0, \ldots, \kappa\}$ corresponds to the number of irregular curves used ($\kappa = 3$ in our experiments) and $a\%b$ is the remainder of the division of a by b. $q = (1/2) \cdot (r_m^{(p)} + ((r_M^{(p)} - r_m^{(p)}) \cdot \nu) + r_m^{(i)})$ and $c_i^{(c)} = c_m + (c_M - c_m) \cdot u_i$, being ν the pupil aperture and u_i a realization of $U \sim \mathbb{U}(0, 1)$, and $[c_m, c_M]$ the intensity range ([64, 200] in our experiments). a_h and a_v are given by:

$$a_h = j \cdot \frac{r_M^{(i)} - q}{3} + \rho_i + q \qquad (15)$$

$$a_v = j \cdot \frac{r_m^{(i)} - q}{3} + \rho_i + q. \qquad (16)$$

The set of 3-D coordinates $\{(x_{ij}^{(c)}, y_{ij}^{(c)}, z_{ij}^{(c)})\}$ defines the collarette surface, where $(x_{ij}^{(c)}, y_{ij}^{(c)})$ specify the position and $z_{ij}^{(c)}$ determines the transparency at the corresponding point. Finally, each element of $\{(x_{ij}^{(c)}, y_{ij}^{(c)})\}$ is associated to a color $C_{\cdot}$, i.e., $z_{ij}^{(c)} \cdot C_v$, being v a realization of U.

B. Sclera

Multiple layers were created to simulate the depth of vessels inside the sclera, each one blurred by a Gaussian kernel. Let $U \sim \mathbb{U}(3, 10)$. x_i are regularly spaced values in $[0, u]$ interval. i.e., $x_i = i \cdot (1/2^{u-1})$, being u a realization of U. Let $y_i = u_i$, being u_i a realization of a uniform distribution in $[-(s_h/2^{1+u})(s_h/2^{1+u})]$ interval and $c_i = v_i$, where v_i is drew from a Uniform distribution in $[0, n/2]$ interval (n is the total number of intensities). o_x and o_y are random offsets drew from Uniform distributions in $[-(s_h/2^4), s_h/2^4]$ and $[-(s_v/2^4), s_v/2^4]$ intervals. Let θ_k be regularly spaced angular intervals $\theta_k = (k/t) \cdot 2\pi$, $k \in [0, t]$, where t is the number of veins per layer. Let $a_k^{(0)}$ be sampled from a Uniform distribution in $[-(s_h/2^4), s_h/2^4]$ interval. The following terms are obtained:

$$a_{ik}^{(1)} = a_k^{(0)} + \sqrt{\left(r_M^{(i)} \cdot \cos(\theta_k)\right)^2 + \left(r_m^{(i)} \cdot \sin(\theta_k)\right)^2} \qquad (17)$$

$$a_{ik}^{(2)} = \sqrt{\frac{s_h}{2}^2 + \frac{s_v}{2}^2} - a_{ik}^{(1)} \qquad (18)$$

$$a_{ik}^{(3)} = a_{ik}^{(1)} + a_{ik}^{(2)} \cdot x_i. \qquad (19)$$

Based on $a_{ik}^{(3)}$, the coordinates of the sclera veins are given by:

$$x_{ik}^{(v)} = \frac{s_h}{2} + o_x + a_{ik}^{(3)} \cdot \cos(\theta_k) - y_i \cdot \sin(\theta_k) \qquad (20)$$

$$y_{ik}^{(v)} = \frac{s_v}{2} + o_y + a_{ik}^{(3)} \cdot \sin(\theta_k) + y_i \cdot \cos(\theta_k). \qquad (21)$$

Finally, the set of coordinates $\{(x_{ik}^{(v)}, y_{ik}^{(v)})\}$ is associated to a color $c_{ik} = C^{(v)}$, being $C^{(v)}$ the vessel color. Also, the outer region of a circle that spreads along 90% of the image is filled by $C^{(v)}$ and blurred by a Gaussian Filter, to increase the realism near the eye corners. The resulting image is used in the rendering process to represent the cornea.

C. Rendering

Humans are extremely used to observe eyes, which increases the challenge of realistic rendering. Also, due to the diversity of components and of their optical properties, the ocular region is the most difficult part of the face to render realistically. Hence, a 3-D model of a real head was created using a 3-D scanner [15] and the major properties of this model adjusted when rendering each sample.

1) Skin: The skin is specially complex to render due to its translucency: when ray tracing, around 6% of the light is reflected and the remaining penetrates the surface, scatters along its sublayers and approximately 94% exits at a different location [6]. This phenomenon is called *subsurface scattering* (SSS) [22] and was used to simulate the light and skin interaction. The proposed method is a combination of SSS, diffuse, specular and rim lighting. The SSS effect is mainly determined by three texture maps that define the color of each pixel: 1) a color map (Fig. 4(A)); 2) a normal map (Fig. 4(B)); and 3) a SSS map (Fig. 4(C)). The latter defines how regions are affected by translucency. The SSS value $v \in R$ extracted from the SSS map is multiplied by a constant value κ to control the amount of SSS.

Fig. 4. Example of the types of textures used in subsurface scattering: (A) Color map. (B) Normal map. (C) Subsurface scattering map.

This value is added to the dot product between the light vector $\vec{l} \in R^3$ and the normal vector $\vec{n} \in R^3$, obtained from the normal map (Fig. 4(B)) yielding the SSS value:

$$s_s = \kappa \cdot v + \frac{\vec{n}}{\|\vec{n}\|} \cdot \frac{\vec{l}}{\|\vec{l}\|}, \tag{22}$$

where κ is a regularization term that determines the strength of the subsurface scattering effect ($\kappa \in [0.95, 1.05]$ in our experiments).

The diffuse lighting value d_l yields from the interpolation between the melanin color $m_c \in R^3$ and the color map $c \in R^3$ (Fig. 4(A)), so that the dot product between the normal vector $\vec{n}$ and the light vector $\vec{l}$ is inversely correlated to the melanin color, i.e., $m_c = c \cdot s_s$. Next, the dot product is scaled by the SSS falloff $s_f \in R$, determining the smoothness of the transition from the diffuse to the melanin color. This value is multiplied by $s_s \in R^3$, in order to add the SSS effect to the diffuse color and darken shadowing areas:

$$d_l = \left[m_c + \left((c - m_c) \cdot \frac{\left(\frac{\vec{n}}{\|\vec{n}\|} \frac{\vec{l}}{\|\vec{l}\|} \right)^{s_f}}{\|c - m_c\|} \right) \right] s_s. \tag{23}$$

To determine the specular level, the halfway angle θ_h is initially obtained, by adding the light $\vec{l} \in R^3$ and camera position $\vec{e} \in R^3$ vectors. The direction and amount of light on each segment of the surface is given by $\vec{d} = \theta_h \cdot \vec{n}$, being $\vec{n} \in R^3$ the vector normal to the surface. Next, the gloss is obtained by multiplying the normal texture's alpha channel by a gloss multiplier constant κ_g. The specular value yields from the multiplication of the normal texture's alpha channel by a specular multiplier constant κ_s. The final specular value is given by $s_l = c_s \cdot ((\vec{d}^{\kappa_g} \cdot \kappa_s) \cdot \vec{d})^{\kappa_g}$, being $c_s \in R^3$ the specular color.

To determine the rim lighting color, the dot product between the light $\vec{l}$ and the eye vectors $\vec{e}$ is obtained (which equals -1 when facing the light directly). Then, the dot product between the normal vector $\vec{n}$ and the view or eye vector $\vec{e}$, raised to the rim lighting power $r_p \in R$, controls the power of the rim light. A bias value $\kappa_r \in R^3$ determines the initial value of the rim light value and assures that the dot product between $\vec{n}$ and $\vec{e}$ have different signals on front-side and backside. Finally, these two elements are multiplied, yielding the rim lighting value:

$$r_l = \left[(-\vec{e} \cdot \vec{l} + 1) \cdot r_c \right] \cdot \left[(\vec{n} \cdot \vec{e})^{r_p} + \kappa_r \right], \tag{24}$$

where $r_c \in R^3$ is the rim lighting color. Based on the diffuse d_l, rim r_l and specular s_l lighting values, the final color is given by:

$$f_c = ((s_l + (d_l + r_l)) \cdot c_a) \cdot c_l, \tag{25}$$

being c_l the light color and c_a the alpha value of the color map.
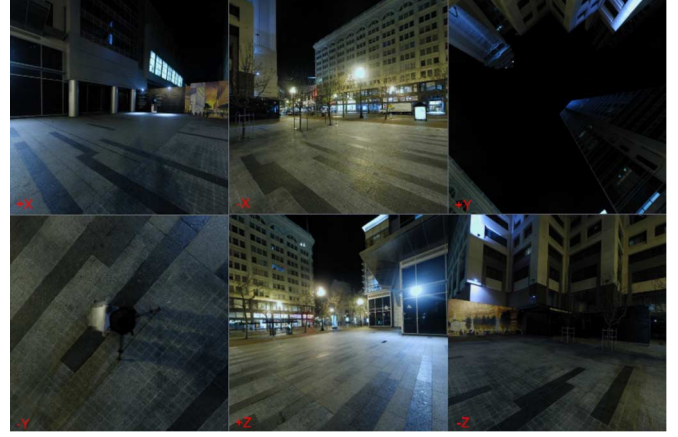

Fig. 5. Example of one cube map used to simulate the environment surrounding the model.

2) Eyes: The eyes are synthesized by ambient reflection, light reflection and refraction techniques, considering that they are highly reflective with respect to the surrounding environment. As illustrated by Fig. 5, cube maps were used to represent the surrounding environments. The ambient reflection is calculated in two steps: 1) multiplying the ambient color $c_a \in R^3$ by the eye color $e_c \in R^3$; and 2) dividing the ambient texture $a_t \in R^3$ by the reflection contrast value $\kappa_r \in R$, which determines the amount of reflection used.

$$a_l = c_a \cdot e_c + \frac{a_t}{\kappa_r} \tag{26}$$

The color of the eye is determined by the diffuse d_l and specular s_l lighting values. The specular component of lighting is obtained separately for the iris and cornea, due to their specific reflectance properties. The dot product between the normal vector $\vec{n}$ and the light position vector $\vec{l}$ represents the direction and amount of light at this point of the surface. The diffuse color is given by $c_d = e_c \cdot \vec{n} \cdot \vec{l}$. Then, a constant κ_b controls the power of the diffuse color:

$$d_l = \frac{c_d + \kappa_b}{\|c_d + \kappa_b\|}. \tag{27}$$

To obtain the specular value for the cornea and iris, the halfway vector between the viewer and light source is initially obtained by summing the light $\vec{l}$ and eye $\vec{e}$ vectors. The power of the specular level for the cornea is controlled by a constant gloss factor κ_g. As the cornea strongly reflects the surrounding environment, ambient specular reflection was added to the specular calculation by multiplying the specular level by the reflection cube map texture $t_c \in R^3$:

$$s_c = \left(\frac{Nc}{\|Nc\|} \cdot \frac{\vec{l} + \vec{e}}{\|\vec{l} + \vec{e}\|} \right)^{\kappa_g} \cdot t_c \tag{28}$$

The specular value for the iris s_i is yielded similarly, except that a normal vector from the iris is used. Considering that the iris should have a specular reflection close to the color of the iris, the specular level for the iris was multiplied by the alpha channel of the normal texture and also by the eye color e_c value. The final specular value corresponds to the sum of the specular values for

TABLE II
SUMMARY OF THE DATA VARIABILITY AND DEGRADATION FACTORS
IN NOISYRIS IMAGES THAT SIMULATE THE ACQUISITION OF IRIS
DATA IN UNCONTROLLED CONDITIONS

Factor	Range
Illumination Amount	$[2E^{-3}, 1.000]$ lux
Number of Light Sources	$[1, 100]$
Type of Illumination	{Spot light, Sun light, Point light}
Pupillary dilation	$[r_i/4, r_i/2]$, r_i=major iris radius
Gaze Yaw	$[-30°, 30°]$
Gaze Pitch	$[-30°, 30°]$
Pose Yaw	$[-30°, 30°]$
Pose Pitch	$[-30°, 30°]$
Acquisition distance	$[1m, 8m]$
Iris occlusions	$[0\% - 100\%]$
Optical defocus	$[0 - 3]$ σ Gaussian kernel
Motion blur	$[0 - 1]$ m/s
Environments	{1-8}
Glasses	{Yes, No}

the iris and cornea $s_l = s_i + s_c$. The final eye color yields from adding the specular and diffuse lighting values, multiplied by the light color, i.e., $s_l + d_l \cdot l_c$. Eyelashes are represented by a UV mapped curvilinear surface, rendered with transparency. An anti-aliasing technique Fast Approximate Anti-Aliasing [11] is used to soften the eyelashes, blending the edge pixels. In order to create the eye opening and eye moving movements, a facial animation rig for the eyes and eyelids is created using skeletal animations. The animations are finally blended, in order to use them simultaneously.

IV. DATA VARIABILITY AND DEGRADATION FACTORS

As stated above, one of the key distinguishing features of the NOISYRIS data is the simulation of uncontrolled acquisition conditions. Table II summarizes the data variability and degradation factors that were implemented, with corresponding variation/degradation intervals: 1) *Optical defocus*: while a camera lens is focusing at a distance, a gradual decrease in sharpness is apparent in its surroundings. This effect is called Depth of Field (DoF) and refers to the region that appears sharp in the image. The DoF varies according to the camera and focusing distance as well as other variables; 2) *Motion blur* occurs while acquiring data from moving sources. Even slight movements of the subjects can lead to motion blurred data; 3) *Iris occlusions* are among the most concerning factors for recognition effectiveness, because different types of objects can occlude large portions of the iris rings (e.g., eyelids, eyelashes, and hair); 4) *Varying gaze*: images possess varying 3-D angles between the camera and the subject's gaze. These variations are especially relevant because they transform the iris boundaries into ellipses and increase the challenges of the segmentation and normalization phases; 5) *Varying pose* occurs in a similar way to varying gaze. The subjects might not be in front of the camera during data acquisition, which raises challenges for recognition algorithms, often requiring pose compensation techniques; 6) *Varying distances*: acquisition from different distances was simulated to obtain data with differences in scale; 7) *Varying lighting conditions* are especially relevant in the case of ocular images because of the glossy/specular reflections in the iris that are determined by the lighting conditions in the environment

that surrounds the subject. A varying number of light sources were simulated, with varying intensities and types of light, inside various environments; 8) Different levels of *iris pigmentation* were simulated, which are particular important in the amount of texture visible in VW data; and 8) *Glasses*, which are an especially difficult factor in terms of recognition effectiveness, because lenses might introduce nonlinear deformations in the appearance of the iris texture.

Fig. 6 illustrates the variability and degradation factors implemented. In this case, for clarity of visualization, images were selected to emphasize each factor independently. In practical terms, images are usually degraded by more than one factor simultaneously.

V. DATA VALIDATION: EXPERIMENTS

A. Amount of Information

The first empirical evaluation of the NOISYRIS data comprised the assessment of the amount of information in local patches of the irises I_p represented in grayscale and in the polar domain, by assessing their entropy $h()$:

$$h(I_p) = \sum_i p(i) \cdot ln\left(p(i)\right). \tag{29}$$

Here, $p(i)$ is the probability of a pixel intensity in the $[0, 255]$ interval. For reference, the values obtained were compared to similar statistics that were drawn from the UBIRIS.v1 [16] data set. This analysis was motivated by the Gabor-based feature encoding scheme suggested by Daugman [3]: "*local patches are projected onto quadrature Gabor wavelets, generating complex-valued coefficients whose real and imaginary parts set two bits of the biometric signature*." The results are given in Fig. 7: the left side of the figure shows the density of the $h(I_p)$ values for the two image examples, in which the continuous line pertains to a UBIRIS.v1 image and the dashed line pertains to a NOISYRIS image. The right side plots show summary statistics comprising the $h(I_p)$ means (μ) and the standard deviations (σ) of the densities of the set of compared images. The results confirm the similarity between the summary statistics (μ, σ) that were obtained for the data set of real irises (upper plot) and the NOISYRIS data (bottom plot).

B. Between-Class Variability

Iris distinctiveness was measured not only in terms of recognition performance but also by estimating the degrees of freedom of the biometric signatures. Furthermore, we assessed to what extent distinctiveness results from the intrinsic features of the texture of the iris or the environmental conditions during image acquisition. Sets of irises from different subjects were initially generated without considering any visualization artifacts, and the corresponding biometric signatures were extracted using the Gabor kernel: wavelength $\omega = \sqrt{2}$, orientation $\theta = \pi/2$, phase $\phi = 0$, and ratio $\alpha = 1$. The rendering variability was also considered (lighting conditions, gazes, angles, and pupillary dilations) for the same set of irises. Finally, in an *all-against-all* scheme, signatures were compared and the proportion of mismatched bits was calculated. The results are given in Fig. 8 and are divided into two sets. The white bars

Fig. 6. Illustration of the data variability and degradation factors that were simulated to resemble the characteristics of the data that were acquired in noncontrolled setups. For the purposes of illustration, each degradation factor occurs in an isolated manner in these examples.
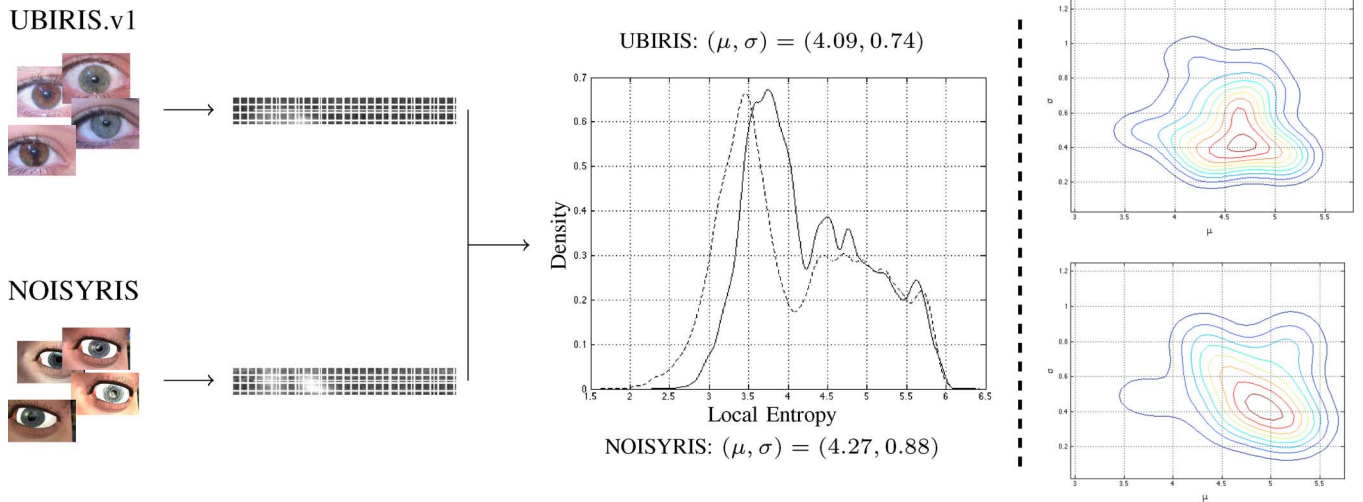

Fig. 7. At left, example of the differences between the estimates of the entropy value densities in the local patches (size $\omega \times \omega, \omega \approx 5 \times$ Gabor kernel wavelength) of a real (continuous lines) and a synthetic (dashed line) iris image. At right, the contour plots of the mean and standard deviation values (μ, σ), the bivariate densities, which were observed for a set of 1,000 images of the UBIRIS.v1 data set (top plot), and 1,000 NOISYRIS images (bottom plot).

denote the results that were observed when only the intrinsic distinctiveness of the iris texture was considered, meaning that the variability factors in the rendering were not introduced. The histogram in red bars represents an experiment that considered all of the types of variability factors, allowing us to evaluate the roles of the intrinsic and environmental factors. Based on this experiment, we concluded that most of the distinctiveness of an iris stems from the texture synthesis phase. Moreover, the rendering factors slightly increase the average differences between

the iris textures and slightly increase the standard deviation of the resulting distribution. As expected, these relationships also increase the number of degrees of freedom in the distribution that occurs in a later experiment, described below.

C. Within-Class Variability

Fig. 9 illustrates what aspects of within-class variability stem from biological (pupillary dilation, occlusions, and nonlinear local deformations) and environmental (lighting, poses, angle
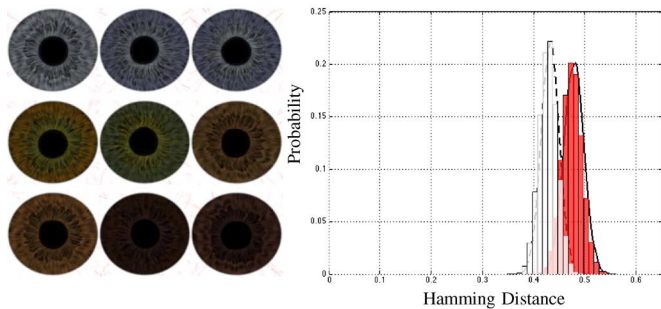
Fig. 8. Left: close-up of irises that were generated for nine different subjects. Right: density estimate for the *all-against-all* comparison between irises of 10^4 different subjects, in which the variability of the iris patterns (white bars) were considered exclusively and in conjunction with the rendering variability factors (red bars).
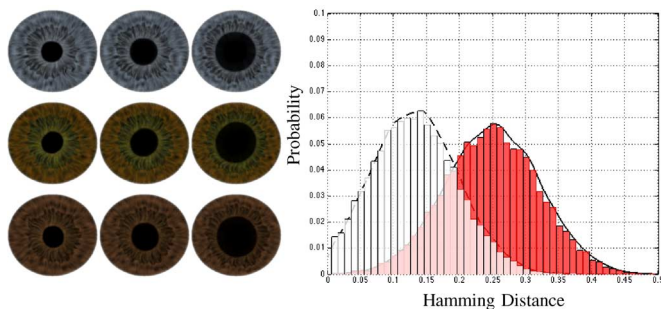

Fig. 9. Left: close-up of three iris samples from three subjects with different levels of pupillary dilation. Right: estimate of the within-class variability with respect to the families of parameters described in Sections III-A (white bars), III-C, and IV (red bars).

distances, and levels of focus) factors. The white bar histogram represents the former and the red bar histogram gives the bit-wise distances when both the biological factors and the environmental factors are considered. From these plots, it can be concluded that both biological and environmental factors play important roles in the within-class variability of the appearance of an iris. Moreover, the standard deviation slightly increases when both biological and environmental factors are considered; these factors also occur together in images of real irises that are acquired in uncontrolled conditions. Finally, it should be stressed that the average dissimilarity can be fully controlled by parameterizing the biological and environmental factors when creating each data set. In the Appendix, further details are given on accession of the automatic generation framework.

D. Iris Segmentation

This study aims to provide data for different phases of iris biometrics analysis. Hence, it is important to observe how a state-of-the-art iris segmentation algorithm performs with synthetic data, allowing a comparison with segmentation performance on real data. For this purpose, the approach of He *et al.* [7] was selected for two reasons: 1) It is considered to be a state-of-the-art segmentation algorithm and is widely reported in the specialized literature; and 2) It was the algorithm that performed best in the NICE.I contest [17], which specifically examined handling degraded iris data. The results are given

in Fig. 10. At the right side of Fig. 10, a boxplot of the bit-wise dissimilarities between the output of the segmentation algorithm and the ground-truth segmentation data is given (manually constructed in the case of UBIRIS and automatically generated for NOISYRIS). The results appear to be close, especially the median and the first and third quartile values. Outliers correspond most often to cases in which the segmentation algorithm failed to define the region-of-interest and compromised the subsequent segmentation process. In this case, a slightly lower error rate was observed for synthetic data, which is explained by the reduced variability in the periocular region of these images, resulting in an easier segmentation task. The lower variance in segmentation accuracy that was attained for the synthetic data is confirmed by a comparison of the lower interquartile and whiskers ranges with results from the analysis of real images. However, the segmentation algorithm handled the synthetic iris data acceptably without any additional parameterization, which can be regarded as a strong indicator of the quality of the NOISYRIS data.

E. Iris Recognition Performance

Finally, recognition effectiveness on the NOISYRIS data was compared to the performance attained on real VW images in two ways: 1) using the classical Gabor-kernel decomposition and Hamming distance matching; and 2) using state-of-the-art iris recognition methods that were specifically devised for VW data.

To use the Gabor/Hamming performance evaluation procedure, a set of 10,000 images was generated (1,000 subjects, with 10 samples per subject), the corresponding *iriscodes* were extracted, and bitwise comparisons were performed in an *all-against-all* scheme. The resulting scores were divided into genuine and imposter sets whether or not they corresponded to samples from the same eye. These experiments were performed in accordance with the widely used strategy proposed by Daugman [3]. The Gabor configurations used resulted from exhaustive evaluation, including testing combinations of the wavelength ω, orientation θ, phase ϕ, and ratio α parameters, to arrive at the final configuration ($\omega = \sqrt{2}$, $\theta = 0$, and $\pi/2$, $\alpha = 1$). The results are given in Fig. 11 and agree with the results obtained in uncontrolled environments and with the VW data. When compared to the imposter distribution, the genuine distribution is left-shifted consistently and is substantially broader. The decidability $d' = (\mu_I - \mu_G)/\sqrt{0.5(\sigma_G^2 + \sigma_I^2)}$ was approximately 3.52, with μ_G and μ_I as the means for the genuine and imposter comparisons, and σ_G, σ_I represent the corresponding standard deviations. The fact that the observed mean value for the imposter distribution was slightly lower than the value reported by Daugman [4] was justified because the Gabor codification scheme uses a single type of kernel instead of a combination of multiple kernels, increasing the decidability of the pattern recognition system. Moreover, the fact that no shifts in the iris templates were performed during the signature matching process also decreased the decidability score.

A comparison of the results obtained by the state-of-the-art iris recognition process on the UBIRIS.v2 data and the NOISYRIS synthetic images was conducted on the set of 10,000 images used in the previous evaluation procedure.
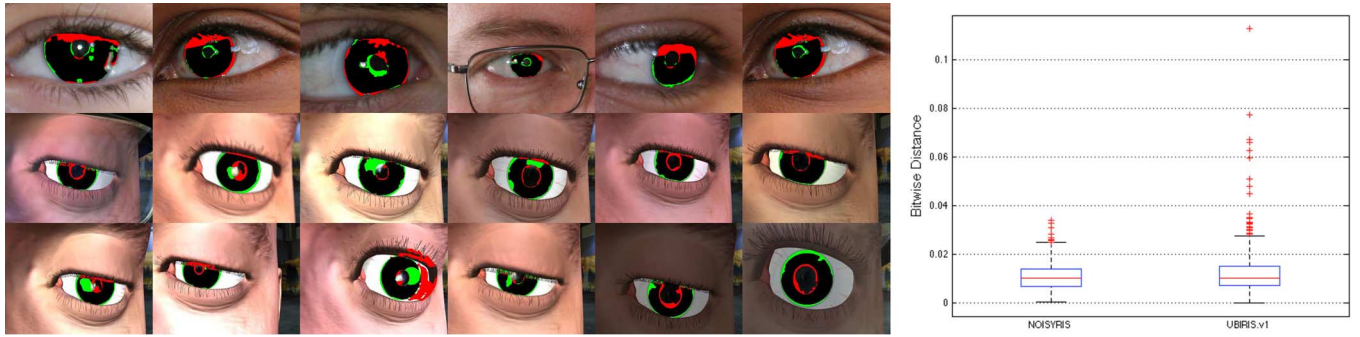
Fig. 10. Left side: examples of misclassified pixels in segmenting images of the UBIRIS.v1 (top row) and NOISYRIS (middle and bottom rows) data using the method proposed by He [7]. The pixels in red (and green) denote false positive (and false negative) cases, respectively. At right, misclassification rates that were obtained by each algorithm on both data sets.
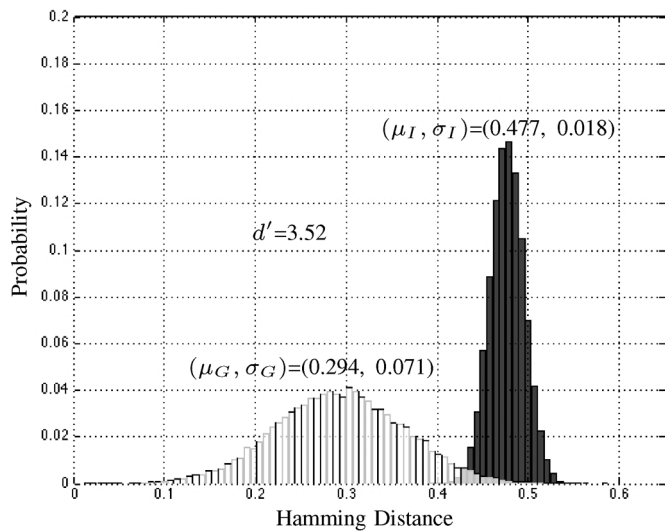

Fig. 11. Decision environment for iris recognition on the NOISYRIS data. The histogram of genuine scores is denoted by white bars, and the histogram of the imposters is represented by dark bars.

The four recognition techniques that performed best in the NICE:II contest were selected because of their performances and because they are validated software implementations of the corresponding techniques. The methods were from Tan *et al.* [24], Wang *et al.* [26], Santos and Hoyle [20], and Shin *et al.* [23]. The results are given in the two ROC plots of Fig. 12, in which the results obtained on the real iris data appear as continuous lines and white markers and the results obtained on the NOISYRIS data are represented by dashed lines and black markers. Results are given in terms of the relationship between the true positive rate (TPR) and the false positive rate (FPR). The ROC analysis reveals that the results in real and synthetic data for the methods of Wang *et al.* and Shin *et al.* are highly similar, which was positively regarded with respect to the quality of the synthetic iris textures. In contrast, the results from the approaches of Tan *et al.* and Santos and Hoyle were not as similar, which can be explained by the fact that these methods also extract information from the periocular region during the recognition process. As described above, the components of the periocular region (especially the eyebrows
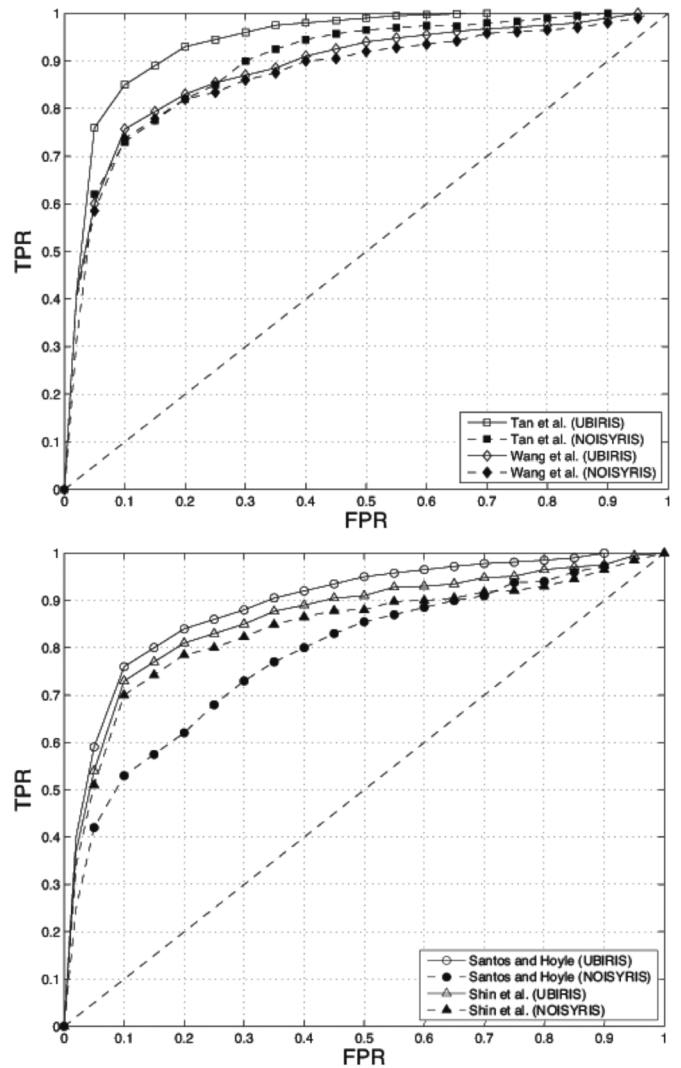

Fig. 12. ROC curves obtained by the four best-performing methods of the NICE:II recognition contest for real iris data (UBIRIS.v2, continuous lines) and NOISYRIS images (dashed lines). The markers denote the corresponding algorithms.

and skin) of the NOISYRIS data are not fully discriminant between individuals, which reduced recognition performance.

VI. Conclusion

When considering the efforts undertaken to perform biometric recognition under uncontrolled conditions, it is especially important for researchers to possess data sets that enable experiments under such conditions. Because of privacy concerns, it is difficult to collect a sufficient amount of data under such conditions. In this paper, a method that synthesizes ocular data is proposed. When compared to similar initiatives, the main concern of this method is the simulation of uncontrolled acquisition conditions that lead to degraded data: optically defocused, motion blurred, off-angle, and occluded data, with nonhomogenous changes in the lighting and shadows. The generated data were empirically validated by state-of-the-art iris segmentation and recognition methods. The results obtained allowed us to confirm that the generated data faithfully reproduce the primary properties of real iris data that are acquired under similar conditions. Moreover, the availability of an online framework that can generate degraded ocular data is described here; this framework is useful for the development and robustness evaluation of iris recognition algorithms.

At present, efforts have concentrated on the within-class and between-class variability of iris patterns. Further work should focus on the synthesis of the main components in the periocular region: skin texture and eyebrow models, and in the increase of the variability of eyelashes and eyelids shapes. These variations are especially important for the evaluation of ocular recognition strategies (e.g., periocular recognition).

As stated in the introduction, the described process involves the synthesis of iris data and the simulation of its acquisition in visible wavelengths. The adaptation of the process to near infrared data would demand a completely different parameterization of all of the texture rendering techniques that have been described ((8) to (21)). In contrast, the techniques that were used to define shapes (e.g., (3) and (5)) would apply similarly to near-infrared data.

Appendix A
List of Colors Used

According to the predominant color of each iris, a set of colors is mixed to the luminosity and transparency effects to generate the color of each iris pixel. We used four main families of eye colors: F_1: blue, F_2: green, F_3 brown and F_4 dark-brown. Below is the list of RGB colors used for each family, represented in hexadecimal format: F_1: {#5C5D79, #8494A4, #B8C3C7, #9DA6A1, #91949B, #676B74}; F_2: {#404E3C, #5D7342, #8A8C3D, #94831A, #8F983B, #7C4A0E, #526023, #607D69}; F_3: {#4F341F, #764F32, #745630, #543516, #977B53, #86572D}; and F_4: {#332113, #211A22, #2B2321, #57372A, #472E27, #5E332D, #3B2532}.

Appendix B
Online Platform

An online platform is available at http://iris.di.ubi.pt/NOISYRIS. Each user has the possibility to adjust the levels of variability for each factor, enabling the simulation from constrained to totally unconstrained acquisition conditions.
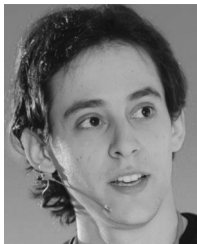
References

[1] K. Bowyer, K. Hollingsworth, and P. Flynn, "Image understanding for iris biometrics: A survey," *Comput. Vis. Image Understand.*, vol. 110, no. 2, pp. 281–307, 2008.

[2] J. Cui, Y. Wang, J. Huang, T. Tan, and Z. Sun, "An iris image synthesis method based on PCA and super-resolution," in *Proc. 17th Int. Conf. Pattern Recognition, 2004 (ICPR 2004)*, Aug. 23–26, 2004, vol. 4, pp. 471–474.

[3] J. Daugman, "The importance of being random: Statistical principles of iris recognition," *Pattern Recognit.*, vol. 36, pp. 279–291, 2003.

[4] J. Daugman, "How iris recognition works," *IEEE Trans. Circuits Syst. Video Technol.*, vol. 14, no. 1, pp. 21–30, Jan. 2004.

[5] M. Dobes and L. Machala, UPOL Iris Image Database, Palacky University in Olomouc, 2004 [Online]. Available: http://phoenix.inf.upol.cz/iris/

[6] C. Donner and H. Jensen, "Light diffusion in multi-layered translucent materials," *ACM Trans. Graphics*, vol. 24, no. 3, pp. 1032–1039, 2005.

[7] Z. He, T. Tan, Z. Sun, and X. Qiu, "Towards accurate and fast iris segmentation for iris biometrics," *IEEE Trans. Pattern Anal. Mach. Intell.*, vol. 31, no. 9, pp. 1670–1684, Sep. 2008.

[8] "CASIA Iris Image Database" Institute of Automation, Chinese Academy of Sciences, 2004 [Online]. Available: http://www.sinobiometrics.com

[9] A. K. Jain, A. Ross, and S. Prabhakar, "An introduction to biometric recognition," *IEEE Trans. Circuits Syst. Video Technol.*, vol. 14, no. 1, pp. 4–20, Jan. 2004.

[10] A. Lefohn, B. Budge, P. Shirley, R. Caruso, and E. Reinhard, "An ocularist's approach to human iris synthesis," *Computer Graphics Applicat.*, vol. 23, no. 6, pp. 70–75, 2003.

[11] T. Lottes, FXAA—Fast Approximate Anti-Aliasing, NVIDIA Corporation, FXAA—White Paper, Feb. 2010.

[12] MMU Iris Image Database, Multimedia University, 2004 [Online]. Available: http://pesona.mmu.edu.my/ccteo

[13] Iris Challenge Evaluation, National Institute of Standards and Technology, 2006 [Online]. Available: http://iris.nist.gov/ICE/

[14] U. Park, A. Ross, and A. K. Jain, "Periocular biometrics in the visible spectrum: A feasibility study," in *Proc. IEEE Int. Conf. Biometrics: Theory, Applications, and Systems*, 2009, pp. 1–6.

[15] L. Perry-Smith, Infinite Realities—3D Head Scan [Online]. Available: http://www.ir-ltd.net/infinite-3d-head-scan-released assessed Sep. 26, 2011

[16] H. Proença and L. A. Alexandre, "UBIRIS: A noisy iris image database," in *Proc. 13th Int. Conf. Image Analysis and Processing*, Sep. 2005, pp. 970–77.

[17] H. Proença and L. A. Alexandre, "Toward covert iris biometric recognition: Experimental results from the NICE contests," *IEEE Trans. Inf. Forensics Security*, vol. 7, no. 2, pp. 798–808, Jun. 2011.

[18] H. Proença, S. Filipe, R. Santos, J. Oliveira, and L. A. Alexandre, "The UBIRIS.v2: A database of visible wavelength iris images captured on-the-move and at-a-distance," *IEEE Trans. Pattern Anal. Mach. Intell.*, vol. 32, no. 8, pp. 1502–1516, Aug. 2010.

[19] A. Ross, S. Crihalmeanu, L. Hornak, and S. Schuckers, "A centralized web-enabled multimodal biometric database," in *Proc. 2004 Biometric Consortium Conf. (BCC)*, Arlington, VA, USA, Sep. 2004.

[20] G. Santos and H. Hoyle, "A fusion approach to unconstrained iris recognition," *Pattern Recognit. Lett.*, vol. 33, no. 8, pp. 984–990, 2012.

[21] S. Shah and A. Ross, "Generating synthetic irises by feature agglomeration," in *Proc. 2006 IEEE Int. Conf. Image Processing*, Oct. 2006, pp. 317–320.

[22] M. Shah, J. Konttinen, and S. Pattanaik, "Image-space subsurface scattering for interactive rendering of deformable translucent objects," *Computer Graphics Applicat.*, vol. 29, no. 1, pp. 66–78, 2009.

[23] K. Shin, G. Nam, D. Jeong, D. Cho, B. Kang, K. Park, and J. Kim, "New iris recognition method for noisy iris images," *Pattern Recognit. Lett.*, vol. 33, no. 8, pp. 991–999, 2012.

[24] T. Tan, X. Zhang, Z. Sun, and H. Zhang, "Noisy iris image matching by using multiple cues," *Pattern Recognit. Lett.*, vol. 33, no. 8, pp. 970–977, 2012.

[25] University of Bath Iris Image Database, University of Bath, 2004 [Online]. Available: http://www.bath.ac.uk/elec-eng/pages/sipg/

[26] Q. Wang, X. Zhang, M. Li, X. Dong, Q. Zhou, and Y. Yin, "Adaboost and multi-orientation 2D Gabor-based noisy iris recognition," *Pattern Recognit. Lett.*, vol. 33, no. 8, pp. 978–983, 2012.

[27] A. Weaver, "Biometric authentication," *Computer*, vol. 39, no. 2, pp. 96–97, 2006.

[28] Z. Wei, T. Tan, and Z. Sun, "Synthesis of large realistic iris databases using patch-based sampling," in *Proc. 19th Int. Conf. Pattern Recognition*, Dec. 2008, pp. 1–4.

[29] Z. Zhou, Y. Du, N. Thomas, and E. Delp, "A new human identification method: Sclera recognition," *IEEE Trans. Syst., Man, Cybern. A, Syst. Humans*, vol. 42, no. 3, pp. 571–583, May 2012.

[30] J. Zuo, N. A. Schmid, and X. Chen, "On generation and analysis of synthetic iris images," *IEEE Trans. Inf. Forensics Security*, vol. 2, no. 1, pp. 77–90, Mar. 2007.

Frutuoso Silva received the B.Sc. degree in mathematics, specialization in computer graphics, from the University of Coimbra, Portugal, in 1992, and the M.Sc. degree in electrical and computer engineering from Technical University of Lisbon-IST, Portugal, in 1997. He received the Ph.D. degree in computer science and engineering from the University of Beira Interior, Portugal, in 2006.

He is currently Assistant Professor of the Department of Computer Science at the University of Beira Interior and leader of the Regain group. His current research interests include geometric modeling, augmented reality, and computer games. He is a member of the Eurographics.

António M. G. Pinheiro (M'99) received the B.Sc. degree in electrical and computer engineering from the Instituto Superior Técnico (I.S.T.), Lisbon, Portugal, in 1988, and the Ph.D. degree from the University of Essex, Essex, U.K., in 2002.

His research interests are focused on image processing, computer vision, and multimedia technology domains. He joined the University of Beira Interior (U.B.I.), Covilhã, Portugal in 1988, where he is currently an Assistant Professor. From 1998 to 2001, he was at the University of Essex, U.K. He was a Portuguese representative of the E.U. Action COST 292 and currently he is a Portuguese representative of the E.U. Action COST IC1003.

Luís Cardoso received the B.Sc. degree in electronics and computers engineering in 2008 and the M.Sc. degree in bionics systems in 2011 from the University of Beira Interior, Covilhã, Portugal.

In his research career, he worked for the research project "NOISYRIS: Synthesis of Noisy Iris Images for Biometric Recognition Purposes" at the SOCIA Laboratory, University of Beira Interior, from 2011 to 2012.

André Barbosa received the B.Sc. degree in computer science in 2009 and the M.Sc. degree in computer science in 2011 from the University of Beira Interior, Covilhã, Portugal.

In his research career, he worked for the research project "NOISYRIS: Synthesis of Noisy Iris Images for Biometric Recognition Purposes" at the SOCIA Laboratory, University of Beira Interior, from 2011 to 2012.

Hugo Proença received the B.Sc. degree from the University of Beira Interior, Portugal, in 2001, the M.Sc. degree from the Faculty of Engineering, University of Oporto, in 2004, and the Ph.D. degree from the University of Beira Interior, in 2007.

His research interests are focused in the artificial intelligence, pattern recognition, and biometrics. Currently, he serves as Assistant Professor in the Department of Computer Science, University of Beira Interior. He is the area editor (ocular biometrics) of the IEEE BIOMETRICS COMPENDIUM JOURNAL and member of the Editorial Board of the *International Journal of Biometrics*. Also, he served as Guest Editor of special issues of the *Pattern Recognition Letters*, *Image and Vision Computing and Signal*, *Image and Video Processing* journals.